MNRAS 000, 1–14 (2023) Preprint 21 December 2022 Compiled using MNRAS LATEX style file v3.0

Main-sequence star super-flares based on entire Kepler data

A.K. Althukair,[1,2]★ D. Tsiklauri,[3]†
[1]Department of Physics and Astronomy, School of Physical and Chemical Sciences, Queen Mary University of London, Mile End Road, London, E1 4NS, UK
[2]Physics Department, College of Sciences, Princess Nourah Bint Abdulrahman University, Riyadh, PO Box 84428, Saudi Arabia
[3]Institute of Mathematics, University of Georgia, 77a Kostava Street, Tbilisi 0171, Georgia

Accepted XXX. Received YYY; in original form ZZZ

ABSTRACT

We wrote and used an automated flare detection Python script to search for super-flares on main-sequence stars of types A, F, G, K, and M in the entire Kepler's long-cadence data from Q0 to Q17 following Shibayama et al. 2013 method. Hence, we extended previous studies by Shibayama et al. 2013, who considered a smaller number of quarters, Q0-Q6, and on G-type dwarfs only. Using these new data, we studied the statistical properties of the occurrence rate of super-flares using three different data-sets, namely, Q0-Q6, Q7-Q17 and Q0-Q17 and provide their inter-comparison. For Q0-Q17 data-set we estimated that a super-flare on G-type dwarfs of energy of 10^{35} erg occurs on a star once every 4360 years. We found 4637 super-flares on 1896 G-type dwarfs. Moreover, we found 321, 1125, 4538 and 5445 super-flares on 136, 522, 770 and 312 dwarfs of types A, F, K and M respectively. We found that the occurrence rate (dN/dE) of super-flares versus flare energy, E, shows a power-law distribution with $dN/dE \propto E^{-\alpha}$, where $\alpha \simeq 2.0$ to 2.1 for all different spectral types from F-type to M-type stars. The similarity of the power-law index values implies that the flares are generated by similar conditions in the underlying physical mechanism, which is believed to be magnetic reconnection. In contrast, the obtained $\alpha \simeq 1.3$ for A-type stars suggests that the flare conditions are different from the rest spectral type stars. We note a general increase in flare incidence rate 4.79 % - 14.04 % in F-type to M-type stars and a slight decrease in flare incidence rate 5.13 % - 4.79 % in A-type to F-type stars. These results are similar to other results, who studied stars with any size, not necessarily the main-sequence, considered here.

Key words: stars: activity – stars: flare – stars: rotation – stars: solar-type – starspots – Sun: flares

1 INTRODUCTION

Flares are unpredictable events defined as a sudden, intense brightening caused by a large burst on the stellar surface as a result of magnetic energy release during the reconnection of twisted magnetic fields in the outer atmosphere of stars, which are typically located above or near star-spots (Shibata & Magara 2011; Walkowicz et al. 2011). Flares produce electromagnetic radiation with a wide range of wavelengths, from long-wavelength radio waves to short-wavelength gamma rays Davenport (2016).

In general the importance of Solar flares is due to their potential hazard to humankind, particularly damages to space technology such as satellites and terrestrial electrical power grids and pipelines via current surges generated by geomagnetic storms in the conductive layers of the Earth. Eastwood et al. (2017) considers an economic impact of space weather including the solar flares. Schulte in den Bäumen et al. (2014) made an estimate for a 1989 Quebec-like event, that the global economic impact would range from 2.4 – 3.4 trillion dollars over a year.

However, the Sun is not the only star on which flares occur. Flares can arise in nearly all main sequence stars with exterior convective envelopes, including both cool and hot stars Pettersen (1989), although they are more common in low-mass stars such as M dwarfs (Walkowicz et al. 2011; Davenport 2016). Stellar flares are thought to be generated by the same process by which solar flares occur through magnetic reconnection Davenport (2016). White light flares are flares in the visible continuum Namekata et al. (2017). White light emission from a solar flare was first seen in 1859 (Carrington 1859; Pitkin et al. 2014; Namekata et al. 2017). Several studies of white-light flares observation were carried out by (Mathioudakis et al. 2003, 2006)

Due to the lack of spatial resolution on stars surfaces, the study of stellar flares is limited to photometry or spectroscopy Walkowicz et al. (2011). Therefore, the Kepler mission made it possible to study stellar flares in detail Van Doorsselaere et al. (2017).

Several studies have been conducted to analyse Kepler data and investigate stellar flares.Walkowicz et al. (2011) discovered 373 flaring stars on 23,000 cool dwarfs in the Kepler Quarter 1 long cadence data using a new flare measure, the photometric equivalent width (EW_{phot}), which expresses the flare energy relative to the star's quiescent luminosity. Their findings suggest that M dwarfs flare more frequently but with shorter durations than K dwarfs and emit more energy. Pitkin et al. (2014) provided a Bayesian method for identifying stellar flares in lightcurve data. The approach is based on the general premise that flares have a distinct form, in which there is a sudden increase with a half Gaussian shape accompanied by an exponential decline. Notsu et al. (2016) searched for super-flares on G-type main sequence stars and detected more than 1500 super-flares on 279 stars using long cadence data from Q0-Q6, and 187 super-flares on 23

★ E-mail: a.k.althukair@qmul.ac.uk
† E-mail: d.tsiklauri@ug.edu.ge

stars using short cadence data from Q0-Q17. Their results show that the occurrence frequency of super-flares (dN/dE) as a function of flare energy (E) follows a power-low function with an index of -1.5. According to their findings, the frequency of super-flares depends on rotation period, with the frequency showing an increase as the rotation period decreases. Yang & Liu (2019b) detected 162,262 flare events on 3,420 flaring stars among 200,000 Kepler targets using long cadence mode (LC) data from data release 25 (DR25).

Davenport (2016) reported the first automated search for stellar flares using the entire Kepler data set of Data Release 24, including long and short cadence data. Approximately 3,144,487 light curves were analyzed for 207,617 distinct objects. Davenport (2016) identified 851,168 flares on 4,041 stars and revealed a strong correlation between flares and the evolution of stellar dynamos as stars age by comparing the amount of activity of the flare with stellar rotation and the Rossby number. Using thresholds for the intensity increase, the increase in the running difference and the flare duration Van Doorsselaere et al. (2017) created a new technique for automated flare detection and applied it to Kepler's long-cadence data in quarter 15. Out of the 188,837 stars in the Kepler field of view during Q15, 16,850 flares have been found on 6662 of them.

Kepler data analysis was not only limited to manual and automated methods, several studies have used machine learning to analyze Kepler data. Vida & Roettenbacher (2018) presented a machine-learning-based code for detecting and studying flares. The code was evaluated on two targets for Kepler and Kepler's second mission (K2) long and short cadence data, respectively. The detected flares for these two targets, as well as their energy, were found to be consistent with earlier findings. Breton et al. (2021) implemented a machine learning analysis pipeline to obtain rotation periods for Kepler targets. The algorithm was used on K and M main-sequence dwarfs studied in Santos et al. (2019), the rotation periods of a sample of 21,707 stars were computed with an accuracy of 94.2%. Machine learning techniques were applied by Ofman et al. (2022) on the TESS datasets to discover exoplanet candidates, by using Kepler data of verified exoplanets as a part of the algorithm training stage and validation.

Shibayama et al. (2013) studied statistics of stellar super-flares. These authors discovered that for Sun-like stars (with surface temperature 5600-6000 K and slowly rotating with a period longer than 10 days), the occurrence rate of super-flares with an energy of $10^{34}-10^{35}$ erg is once in 800-5000 yr. Shibayama et al. (2013) confirmed the previous results of Maehara et al. (2012) in that the occurrence rate (dN/dE) of super-flares versus flare energy E shows a power-law distribution with $dN/dE \propto E^{-\alpha}$, where $\alpha \sim 2$. Such occurrence rate distribution versus flare energy is roughly similar to that for solar flares.

The physical process that adequately describes solar flares is magnetic reconnection. The latter is rapid change of connectivity of magnetic field lines, during which magnetic energy is converted into thermal energy (heating) and kinetic energy of plasma outflows. A general framework of solar flares is well accepted (Masuda et al. 1994; Shibata et al. 1995) however questions such as: (i) how frequently and (ii) under what conditions super-flares occur still remain largely un-answered.

Our motivation is three-fold:

(i) Shibayama et al. (2013) studied statistics of stellar super-flares based on Kepler data in quarters $0-6$ ($Q0-Q6$). Here we would like to investigate how the results are modified by adding more quarters, i.e. what is α power-law for data quarters $7-17$ and $0-17$.

(ii) Shibayama et al. (2013) did not use automated flare detection algorithm. Here we provide a Python script which finds super-flares automatically and only minimal human-eye analysis is needed.

(iii) To study the statistics of stellar super-flares on main-sequence stars of other spectral types A, F, K and M.

Section 2 presents the Kepler spacecraft and its data. Section 3 presents the method used including the targets selection, flares detection, rotation period determination and the flare energy estimation. Section 4 provides the main results of this study. In particular we first reproduce Shibayama et al. (2013) results for $Q0-Q6$, where similar but not identical results are found. Then we extend our analysis to $Q7-Q17$ and $Q0-Q17$. Finally, we present the result of other star spectral types. Section 5 closes this work by providing our main conclusions.

2 KEPLER DATA

Kepler spacecraft was launched in 2009 by NASA to search for exoplanets using the transit photometry method Koch et al. (2010). This spacecraft carried a photometer telescope with an aperture of a 0.95 m and $105^{\circ 2}$ field-of-view (FOV) and designed to stare fixedly at one patch of sky in the constellations of Cygnus, Lyra and Draco, monitoring roughly 200000 stars continuously, to detect changes in brightness caused by planets passing in front of the stellar disc. (Shibayama et al. 2013; Davenport 2016; Yang & Liu 2019b). The Kepler mission had two stages during its lifetime. Kepler's primary mission (K1) which lasted for four years from from 2009 to 2013 when the spacecraft lost two wheels of the four reaction wheels on board. Thus, Kepler's second mission (K2) started in 2014 and carried out until 2018. Due to the problem with the telescope's reaction wheels, it observed around the ecliptic plane. Targets were observed by Kepler using two cadence modes. The long cadence mode (LC) which provide one photometric data point with every 29.4 min, and the short cadence mode (SC) that provide one photometric data point with every 1 min Pitkin et al. (2014). In order to make the Kepler solar panels always to face the Sun, Kepler rotates every 90 days. Thus Kepler's data divided into almost 90-day quarters from quarter 0 to 17 as an abbreviation (Q0 - Q17) except for Q0, Q1, Q8 and Q17, which covers (9, 33, 67 and 32 days respectively). The observational period with the start and end date of each quarter are shown in Table1.

Since the luminosity loss caused by planetary transits is usually less than one hundredth of the star's total brightness, Kepler is intended to obtain high-precision and long-period light curves of many stars Shibayama et al. (2013). As a result, Kepler is considered as a perfect platform to analyse stellar flares due to the significant sample size, the duration of the light curves and the photometric accuracy Davenport (2016).

3 THE METHOD

3.1 Targets selection

We carried out an automated search for super-flares on main-sequence stars type (A, F, G, K, M) based on entire Kepler data, using our bespoke Python script on long cadence data of Data Release 25 (DR 25). The script can be found at `https://github.com/akthukair/AFD` in the filename *AFD.py*. The parameters for all targets observed by Kepler have been taken from The NASA Exoplanet Archive. The algorithm we used based on the method of (Maehara et al. 2012; Shibayama et al. 2013). All Kepler light curve data (2.5 TBytes) were obtained as a fits files from the Mikulski Archive for Space Telescope (MAST) with kind assistance of Deborah Kenny of STScI. Only long cadence targets were selected (with time resolution

Table 1. The observational period T and the start and end dates of each quarter.

Quarter	T (days)	Strat Date (UT)	End Date (UT)
0	9	2009-05-02	2009-05-11
1	33	2009-05-13	2009-06-15
2	88	2009-06-20	2009-09-16
3	89	2009-09-18	2009-12-16
4	90	2009-12-19	2010-03-19
5	95	2010-03-20	2010-06-23
6	90	2010-06-24	2010-09-22
7	90	2010-09-23	2010-12-22
8	67	2011-01-06	2011-03-14
9	97	2011-03-21	2011-06-26
10	93	2011-06-27	2011-09-28
11	97	2011-09-29	2012-01-04
12	83	2012-01-05	2012-03-28
13	90	2012-03-29	2012-06-27
14	97	2012-06-28	2012-10-03
15	98	2012-10-05	2013-01-11
16	86	2013-01-12	2013-04-08
17	32	2013-04-09	2013-05-11

of 29.4 min). Since Kepler's optical aperture has a radius of 4-7 pixels Bryson et al. (2010), and the pixel size of the CCDs is about four arcs Van Cleve & Caldwell (2009), it is thus quite possible that some targets are very close to each other on CCDs, which indicates that nearby star's brightness variations may influence the target star's flux (Shibayama et al. 2013; Yang et al. 2017; Yang & Liu 2019b). Due to this reason we calculated the angular distance between every two stars in the entire sample, which is about 200,000 stars and excluded pairs of neighbouring stars within 12 arcsec from the analysis, to avoid detecting fake flares on the target Shibayama et al. (2013). The overall number of samples that were excluded from the study according to this condition are about 6%. The angular distance θ between two stars was calculated by the following equation:

$$\theta = \cos^{-1}[\sin\delta_1 \sin\delta_2 + \cos\delta_1 \cos\delta_2 \cos(\alpha_1 - \alpha_2)], \quad (1)$$

where α_1 , α_2 , δ_1 , δ_2 are the right ascensions and the declinations of the two stars in degree respectively. We used the Harvard Spectral classification to obtain the spectral type for each target as shown in Table 2. Whereas the effective temperature and radius of main-sequence stars in different spectral type are as follows: $2400 \leq T_{\rm eff} < 3700$, and radius $\leq 0.7\ R_\odot$ for M-type, $3700 \leq T_{\rm eff} < 5200$ and radius of $0.7 - 0.96\ R_\odot$ for K-type, for G-type we used the same effective temperature of (Maehara et al. 2012; Shibayama et al. 2013) which range between $5100 \leq T_{\rm eff} < 6000\ K$ and radius of $0.9 - 1.15\ R_\odot$, F-type has $6000 \leq T_{\rm eff} < 7500\ K$ and radius range between $1.15 - 1.4\ R_\odot$, and A-type has $7500 \leq T_{\rm eff} 10,000\ K$ and radius between $1.4 - 1.8\ R_\odot$ for A-type. Due to the small number of A-type main-sequence stars that fall under these conditions, which makes the statistics inaccurate, we have not implemented radius restrictions for this spectral type. The total number of main-sequence stars is 2222, 10307, 25442, 10898, 2653 for M-, K-, G-, F-, and A-type, respectively.

3.2 Flare detection method

Kepler light curves contain two kinds of flux, the Simple Aperture Photometry flux (SAP) and the Pre-searched Conditioning SAP flux (PDCSAP), which has long term trends removed Davenport (2016). Figure 1 illustrates the difference between these two types of fluxes.

Table 2. The effective temerrature $T_{\rm eff}$, radius and number of stars for each spectral class.

Class	$T_{\rm eff}$ (K)	Radius ($R_\odot$)	$N_{\rm star}$
A	7500 - 10000	1.4 - 1.8	2653
F	6000 - 7500	1.15 - 1.4	10898
G	5100 - 6000	0.9 - 1.15	25442
K	3700 - 5200	0.7 - 0.96	10307
M	2400 - 3700	$\leqslant 0.7$	2222

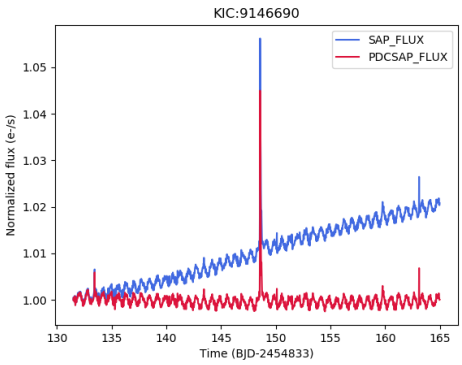

Figure 1. Light curve of KIC 9146690 using two types of flux. The simple aperture photometry flux SAP FLUX (blue) and the pre-searched conditioning SAP flux PDCSAP FLUX (red) which detrends the time variation.

All light curves were analyzed using an algorithm with a similar technique to (Maehara et al. 2012; Shibayama et al. 2013).

A brief description of this method is as follows. In order to be statistically accurate, after generating light curves of all selected stars using the PDCSAP flux, we computed the distributions of brightness variation by calculating the flux difference in adjacent time intervals between every two neighbouring points of all the data points in the light curve. The purpose of this step, as clarified by Shibayama et al. (2013), is to avoid false flare detection and misdetection of short stellar brightness variation and not to overpass large flares. Then, we find such value of flux difference where the area under the distribution is equal to 1% of the entire area. This value indicates a large flux difference between two adjacent points. To enhance the the threshold, we multiplied the 1% value of the area by a factor of three. This threshold value has been chosen by Shibayama et al. (2013) based on multiple tests. Examples of some of the outputs of this method, which give the distribution of brightness variations and the threshold determination, are shown in Figure 2. Figures 2(a) and 2(d) show light curves of KIC 4371489 at Q2 with a rotation period of 1.09 days and KIC 7354508 at Q3 with a rotation period of 17.8 days, respectively. Figures 2(b) and 2(e) show a zoom-in of these light curves, illustrating the rotational periods. Figures 2(c) and 2(f) show the distribution of brightness difference between every two neighbouring points of all the data points in the light curves of KIC 4371489 and KIC 7354508, respectively. The dashed vertical lines indicate 1% of the total area under the distribution curves. The solid vertical lines indicate the threshold values of flares detection, which is equal to three times 1% of the area under the curve. According to Shibayama et al. (2013), the detection threshold depends on the star's rotational period, and its brightness variation amplitude. For short-rotation-period stars (e.g., KIC 4371489), the distribution of brightness variations appears to extend larger than that for long-rotation-period stars (e.g., KIC 7354508). This large extension is because the difference in brightness

between two successive data points is greater in stars with a short rotation periods than in stars with a long rotation periods, resulting in a greater value of flare detection threshold. Also, thresholds in stars with large brightness variation amplitudes are larger than those in stars with small brightness variation amplitudes. We defined the start time of a flare as the time when the flux difference of two consecutive points exceeds the threshold for the first time.

To determine the flare end time, we computed the three standard deviations (3σ) of the brightness variation distribution. We used the relative flux ($\Delta F/F_{\rm avg}$) as shown in Figure 3, where $\Delta F = F_{\rm norm}(t) - F_{\rm avg}$, with $F_{\rm norm}(t)$ being the normalized flux of the light curve, $F_{\rm avg}$ is the normalized flux average, and fitted a B-spline curve through three points distributed around the flare. Each of these three points is an average of five data points distributed as follows, the first average point just before the flare, the second average point around 5 hours after the flare maximum and the third average point around 8 hours after the flare maximum, see Figure 3 (b). The purpose of curve fitting is to remove long-term brightness variations around the flare Shibayama et al. (2013). After subtracting the B-spline curve from the original relative flux as in Figure 3 (c), we define the end time of the flare as the time when the relative flux produced by the subtraction becomes less than the value of 3σ of the distribution for the first time. The flare amplitude is given by:

$$A = \frac{F_{\rm max} - F_{\rm avg_2}}{F_{\rm avg}}, \tag{2}$$

where $F_{\rm max}$ is the normalized flux at the flare peak, $F_{\rm avg_2}$ is the normalized flux average of two points distributed around the flare. The first is the average of five data points before the start of the flare and the second is the average of five data points after the end of the flare, $F_{\rm avg}$ is the normalized flux average.

After selecting the start and end time of each flare, we applied conditions to all flare candidates. These conditions are as follows: the duration of the flare should be longer than 0.05 days, which equals 72 minutes, which means at least 3 data points, and the period of the decline phase of the flare should be longer than the period of the increase phase. Only flare events that satisfy these conditions were analysed Shibayama et al. (2013). After selecting all flares that met the conditions, we checked by eye the light curve for each flare and eliminated false flares. We have not tested the pixel level data of stars showing flares as done in Shibayama et al. (2013) for the reason of simplicity. As can be seen in our results this test omission does not alter overall findings about e.g. flare occurance rate which us found to be similar to Shibayama et al. (2013).

3.3 Rotational period determination

We computed the brightness variation periods of light curves using the Lomb-Scargle periodogram, a common statistical method for identifying and describing periodic signals in unevenly sampled data VanderPlas (2018). We set the oversampling factor (number of samples per peak) in the periodogram to be five VanderPlas (2018) and create a Lomb-Scargle periodogram for each light curve in each quarter from Q2 to Q16 using PDCSAP flux. The light curves data of Q0, Q1 and Q17 were excluded due to their short duration similarly to McQuillan et al. (2014), as shown in Table 1. Further, we assigned the period corresponding to the highest power of the periodogram to be the rotation period for the Kepler ID in a certain quarter. To make the selection of star rotation period automatic rather than manual, we calculated this value with an accuracy of a day without the decimal part since fraction of a day would not significantly affect the results. For periods of less than a day, we set them to 0.5 days, and for periods of less than 0.1 days, we excluded them. According to McQuillan et al. (2014), a good sign of actual astrophysical periodicity is that it can be found in different parts of the light curve. This is because peaks caused by systematics or artefacts are less likely to appear in multiple regions of the light curve. Therefore, in order to choose the accurate rotational period, we have selected the period that is most frequent in all quarters from Q2 to Q16 for each Kepler ID. We then required that the period chosen for all quarters should be identified in at least two distinct segments, following the McQuillan et al. (2014) technique, where the segment is defined as three consecutive Kepler quarters (Q2,Q3,Q4) - (Q5,Q6,Q7) - (Q8,Q9,Q10) - (Q11,Q12,Q13) - (Q14,Q15,Q16). It is worth noting that this method has only been applied to the 1897 Kepler IDs with super-flares that will be considered in 4.1.3. Using the segments technique, we determined the rotation periods of 548 flaring stars of the Kepler sample. In addition, we derived 222 rotation periods based on our most frequent period in all quarters. These selected periods showed significant correlation with those published in previous works. We used Excel's (CORREL) function to calculate the correlation coefficient. Where the correlation coefficient reaches about 0.99 for seven IDs in Yang & Liu (2019a), 0.99 for 70 IDs in Santos et al. (2021), 0.97 for 54 IDs in McQuillan et al. (2014) and 0.95 for 54 IDs in Reinhold & Gizon (2015), and 0.92 for 20 IDs in Nielsen et al. (2013). After comparing the 770 rotation periods that we obtained from both approaches to those periods reported in McQuillan et al. (2014), we found 434 common IDs with a correlation coefficient of 0.85 between their periods. Moreover, 231 common IDs in Nielsen et al. (2013) with a correlation coefficient of 0.94 between their rotation periods. Plots of these correlations are shown in Figure 4, where we used *regplot* function in Seaborn Python library to plot the linear regression model fit to the data. The x-axis in both figures represents the rotation periods obtained by this study. The y-axis represents the periods of rotation published by McQuillan et al. (2014) in 4(a) and Nielsen et al. (2013) in 4(b). In both figures, variables change in the same direction, indicating a significant positive correlation. The rotation periods of 80 stars were obtained from other works, including 67 from McQuillan et al. (2014), 6 from Reinhold & Gizon (2015) and 7 from Santos et al. (2021), while we found that 1,047 stars have no discernible rotation period. This could be due to three reasons as mentioned by Yang et al. (2017): (i) the rotation period is longer than 90 days (a quarter), which makes it difficult (or impossible) to detect them in the star's frequency spectrum; (ii) at the accuracy level of Kepler, the light curve has a small amplitude due to the inclination angle and low activity level; (iii) fast-rotating stars have spots in the poles Schüssler & Solanki (1992), making detecting light variation through rotation hard. The entire results on rotational period determination can be found at `https://github.com/akthukair/AFD`.

3.4 Flare energy estimation

We determined the total energy of each flare from the star luminosity, flare amplitude and its duration, following (Shibayama et al. 2013; Yang et al. 2017).

The star luminosity $L_{\rm star}$, which is the total energy that a star produces in one second, depends on the radius of the star R and the surface temperature $T_{\rm eff}$. This is given by the equation:

$$L_{\rm star} = \sigma_{\rm SB} T_{\rm eff}^4 4\pi R^2, \tag{3}$$

where $\sigma_{\rm SB}$ is the Stefan-Boltzmann constant, $4\pi R^2$ is the entire surface area of the star. Hawley & Fisher (1992); Kretzschmar (2011) found that the continuum emission released by white-light flare is

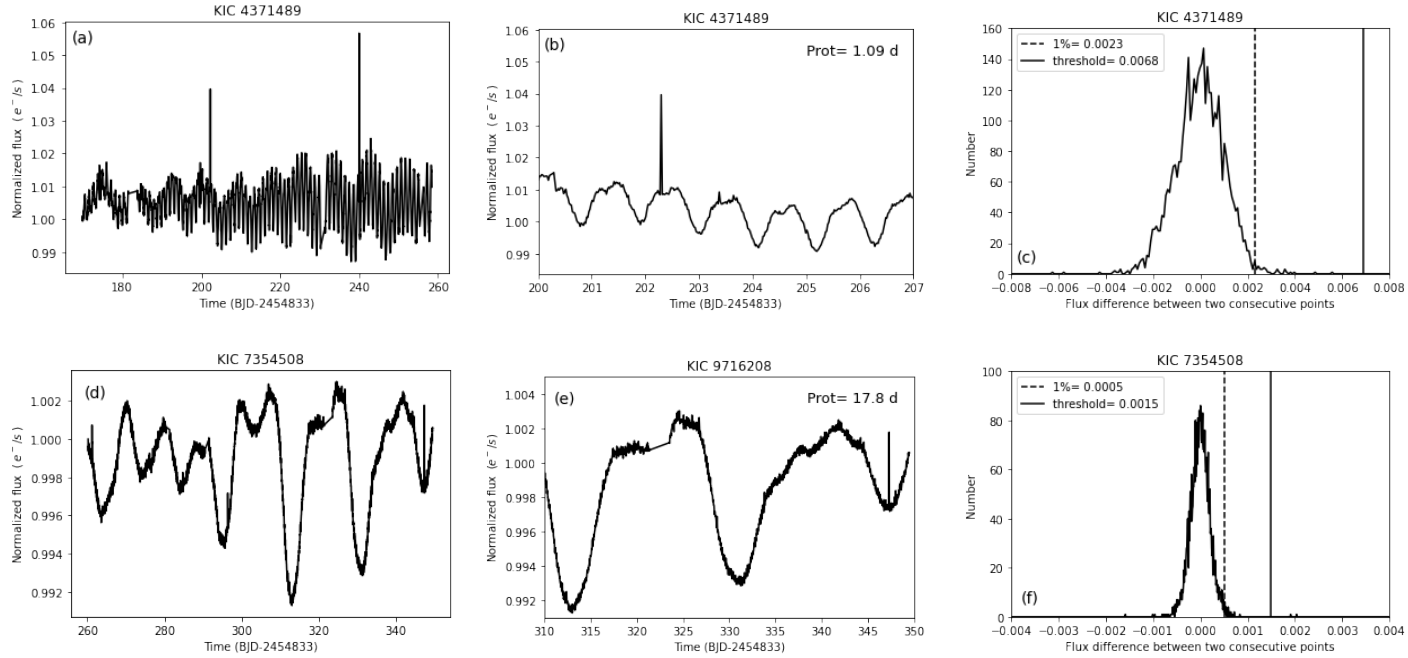

Figure 2. Illustrations of flares detection method used by Shibayama et al. (2013) in both fast and slowly rotating stars. (a) and (d) Show the light curve of KIC 4371489 and KIC 7354508 respectively. (b) A zoom-in into the light curve of KIC 4371489, showing a rotation period of 1.09 days. (e) A zoom-in into the light curve of KIC 7354508, showing a rotation period of 17.8 days. (c) and (f) show the distributions of brightness variation between every two neighbouring points of all the data points in the light curves of KIC 4371489 and KIC 7354508 respectively. The dashed vertical lines denote the value of 1% of the total area under the curve, and the solid vertical lines denote the flare detection threshold.

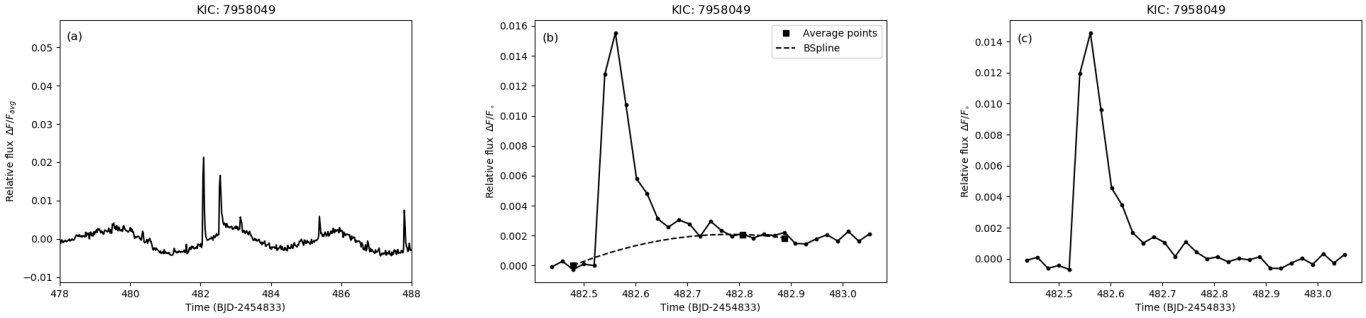

Figure 3. Demonstration of the removal of long-term brightness variations around the flare. (a) Part of KIC 758846 light-curve around the flaring time (10 days of observation). (b) Fitting a B-spline curve (dashed curve) through three points around the flare (squares). The first point is an average of five data points just before the flare, the second point is an average of five data points after 5 h of the peak, and the third point is an average of five data points 8 h after the peak. All three averages are shown as squares. Note that the flux is normalized by the flux just before the flare $F_\circ$. (c) The produced light-curve after subtracting the B-spline curve from the relative flux.

compatible with blackbody radiation at about 9500 K. Therefore, in this study $T_{\rm flare}$ assumed to be 9500 K according to (Shibayama et al. 2013; Yang et al. 2017; Günther et al. 2020) and the luminosity for a blackbody emitting star is giving by:

$$L_{\rm flare} = \sigma_{\rm SB} T_{\rm flare}^4 A_{\rm flare}, \tag{4}$$

where $A_{\rm flare}$ is the area of the flare and can be estimated by the equation:

$$A_{\rm flare} = C_{\rm flare} \pi R^2 \frac{\int R_\lambda B_\lambda(T_{\rm eff}) d\lambda}{\int R_\lambda B_\lambda(T_{\rm flare}) d\lambda}, \tag{5}$$

where $C_{\rm flare}$ is the flare amplitude for the relative flux, R_λ is the response function of Kepler instrument Caldwell et al. (2010). The photometer in Kepler use one broad bandpass range from 420 to 900 nm. $B_\lambda(T)$ is the Plank function at a given wavelength and it is given by:

$$B_\lambda(T) = \frac{2hc^2/\lambda^5}{e^{hc/\lambda kT} - 1}, \tag{6}$$

where h is the Planck's constant, c is the speed of light, T is the temperature of the black body, k is the Boltzmann's constant.
$L_{\rm flare}$ can be calculated by substituting Eq.(5) into (4). Since $F_{\rm flare}$

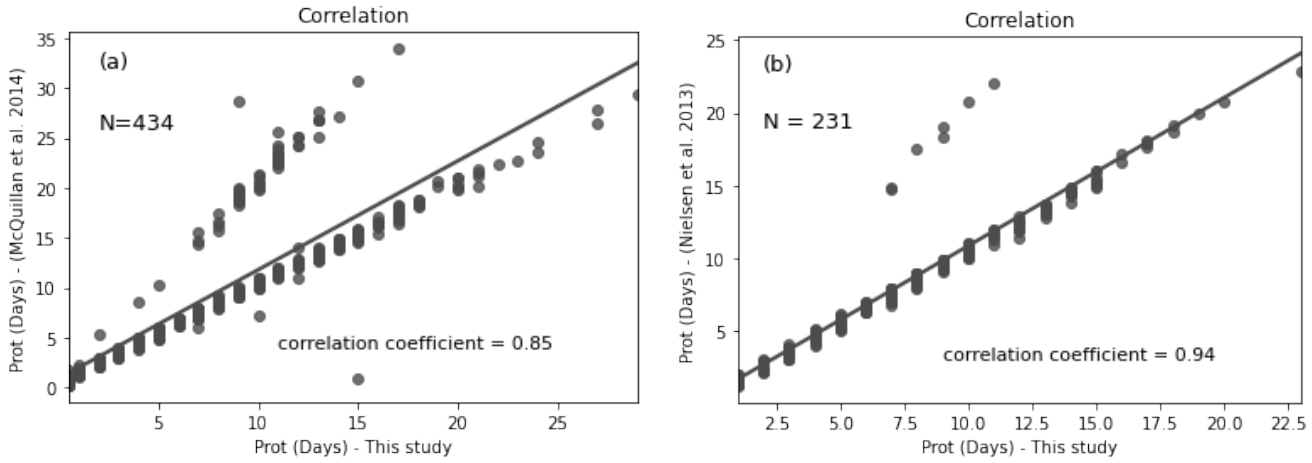

Figure 4. The comparisons of the periods determined in this study to those detected by McQuillan et al. (2014) and Nielsen et al. (2013) in (a) and (b), respectively, reveal a strong positive correlation in which both variables vary in the same direction. The x-axis shows the rotation periods found by this study, and the y-axis displays the rotational periods provided by McQuillan et al. (2014) and Nielsen et al. (2013). N represents the number of stars in each comparison. The correlation coefficient between our periods and McQuillan et al. (2014) is 0.85, while it is 0.94 for Nielsen et al. (2013)

is a function of time, $L_{\rm flare}$ is also a function of time. Therefore, the total energy of the flare is the integral of $L_{\rm flare}$ over the flare duration, and is given by :

$$E_{\rm flare} = \int_{t_{\rm start}}^{t_{\rm end}} L_{\rm flare}(t)dt. \quad (7)$$

4 THE RESULTS

This section presents the main results of this study.

4.1 Super flares on G-type dwarfs

For the benchmarking purposes, we start with the reproduction of Shibayama et al. (2013) results using Q0-Q6 data.

4.1.1 Reproduction of Shibayama et al. (2013) results in Q0-Q6

During 494 days of continuous observation of 25,440 G-type dwarfs, searching for super-flares using Kepler long cadence data, we found 1,298 super-flares on 588 G-type dwarfs. Among them, 229 super-flares on 132 slowly rotating stars. As for the Sun-like stars, which are known as stars with a surface temperature of $5600K \leqslant T_{\rm eff} < 6000K$, a surface gravity of $\log\, g > 4.0$, and a rotational period exceeding ten days Shibayama et al. (2013), we found 151 super-flares on 93 Sun-like stars. The number of detected super-flares in this study is less by 16% than the 1547 super-flares found in Shibayama et al. (2013). In contrast, the number of super-flare stars in this study is approximately 2 times the 279 super-flare stars in Shibayama et al. (2013). Since interstellar activity varies, some stars have shown more than one super-flare, while others have shown only one. In comparison, we found that 161 stars out of 588 have more than one super-flare. While 427 stars showed only one super-flare. The number of Sun-like stars that exhibit more than one super-flare is 18 out of 93. While 75 Sun-like stars showed only one super-flare.

The most energetic super-flare found had an energy of 2.94×10^{36} erg, an amplitude of 0.35 and lasted for about 0.08 days. Figure 5 shows four light curves with a 30-days observation period of the most energetic super-flares that we found with their Kepler ID (left panels). The right panels display a zoom-in of these super-flares, showing their respective energy and their peak time. The black squares on the light curves indicate the data points of the super-flare from the time it starts until it ends.

In Figure 6 are six log-log scale histograms demonstrating the frequency distribution of super-flares in quarters 0 to 6. We estimated the error bar for each bin using the equation:

$$\text{err} = \sqrt{\sum w^2}, \quad (8)$$

where w represents the individual weights of the events that belong in that bin. As a result, when the number of the event in the bin is insufficient, the error bars in statistics are large Shibayama et al. (2013).

Figure 6(a) represents the distribution of the number of observed super-flares per observed flare peak amplitude. The number of observed super-flares is 1298, and the measured amplitude range is approximately between 8×10^{-4} to 3×10^{-1}. Figures 6(b,c and d) show the super-flares frequency distributions as a function of the flare energy. However, each histogram has a different collection of super-flare stars according to the purpose of the comparison. The x-axis indicates the energy of super-flares in erg, and the y-axis represents the number of super-flares per star per year per unit energy. Figure 6(b) show a comparison between frequency distributions of super-flares on all G-type dwarfs (white-solid histogram) and slowly rotating G-type dwarfs with $P_{\rm rot} > 10$ days (grey-dashed histogram). The number of detected super flares is 1298 for all G-type dwarfs and 229 for slowly rotating G-type dwarfs. Since the y-axis is the number of super-flares per star per year per unit energy, we determine the weight for each bin using:

$$w = \frac{3.16 \times 10^7}{N_{\rm os} \times D \times E}, \quad (9)$$

where $N_{\rm os}$ is the number of observed stars, see table 3, D is the duration of the observation period in seconds, and E is the super-flare energy that belongs to that bin. When comparing the distribution of super-flares on all G-type dwarfs and super-flares on slowly rotating G-type dwarfs, we can confirm that the occurrence frequency of super-flares on all G-type dwarfs is higher than the occurrence

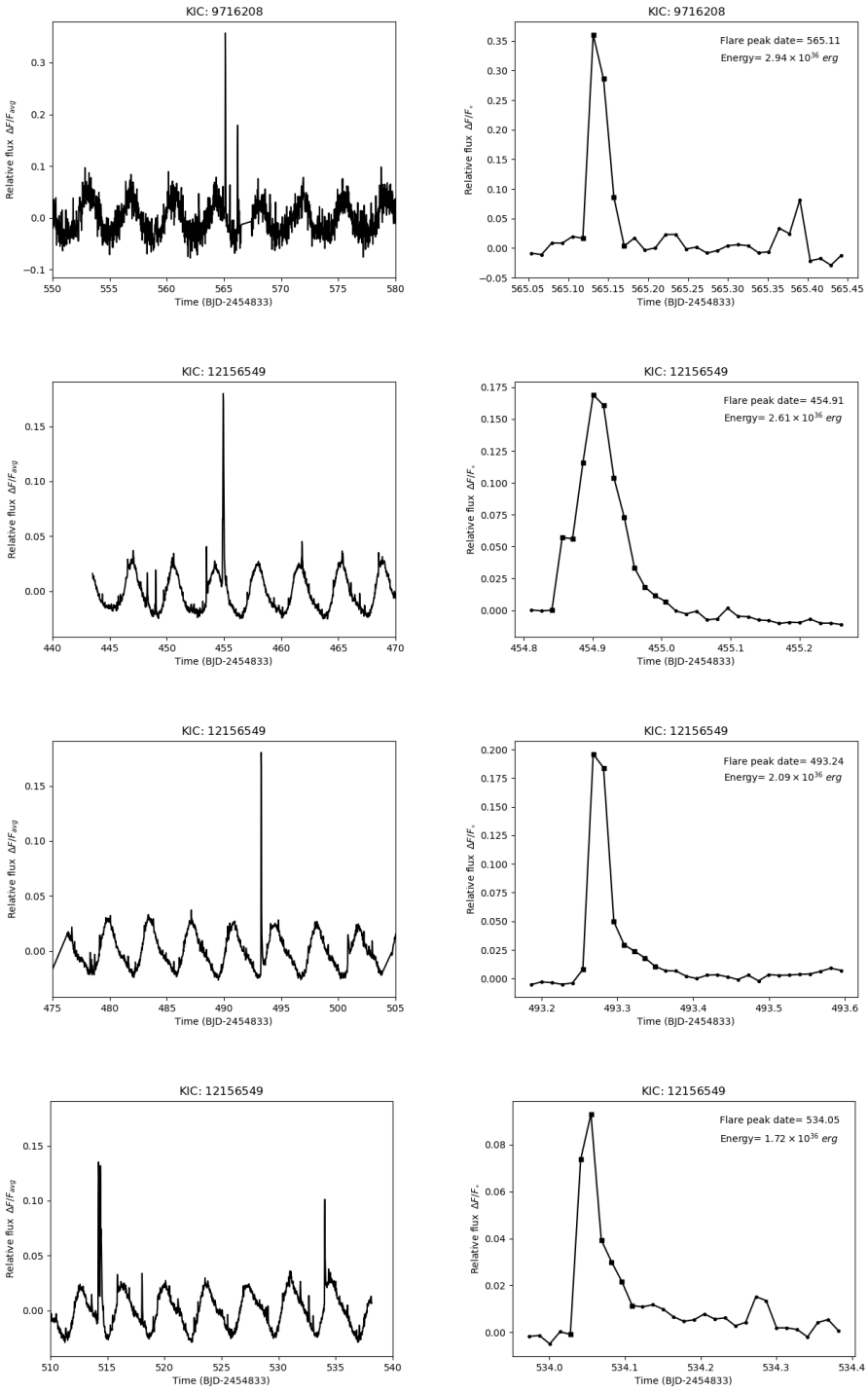

Figure 5. Four of the most energetic super-flares detected during quarter 0 to 6. The left panel shows the light curves of these super-flares over a period of 30 days. The super-flares that occurred on these light curves are enlarged in the right panels. The super-flare energy and peak date are displayed in the upper right corner. The black squares in the right panel correspond to the data points for the super-flares from beginning to end.

frequency of super-flares on slowly rotating G-type dwarfs. Furthermore, it is evident from the two fitted straight lines, (solid line) for all G-type dwarfs and (dashed line) for all slowly rotating G-type dwarfs, that the frequency distributions of super-flares on all G-type dwarfs and slowly rotating G-type dwarfs, follow a power-law relation given by:

$$\frac{dN}{dE} \propto E^{-\alpha}, \tag{10}$$

where the index $\alpha \simeq 2.2 \pm 0.1$ for all G-type dwarfs and $\alpha \simeq 2.0 \pm 0.3$ for all slowly rotating G-type dwarfs. We note that this result is similar to that of Shibayama et al. (2013). Figure 6(c) show the distribution

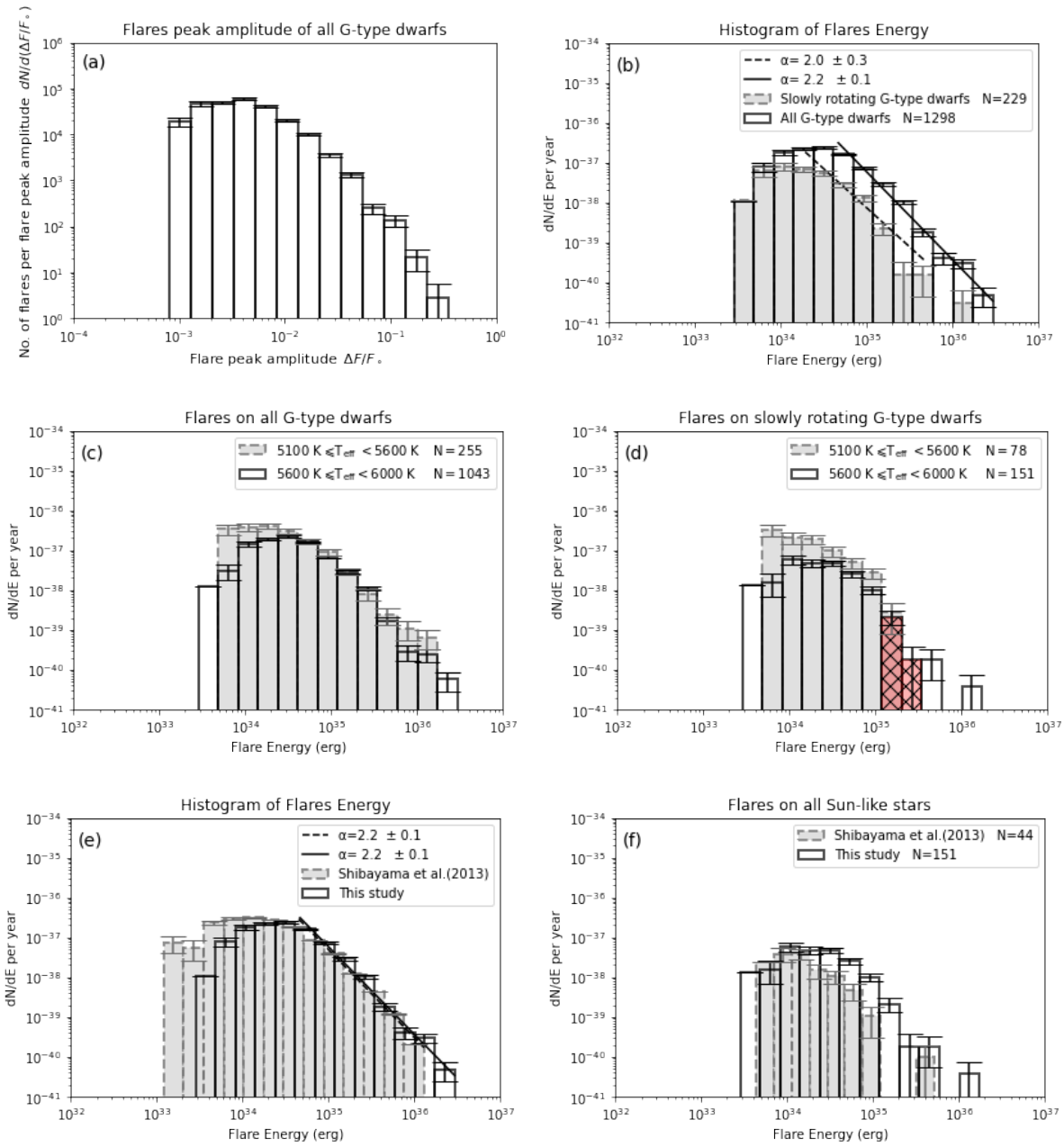

Figure 6. Log-log scale histograms showing the frequency distribution of super-flares on G-type dwarfs ($5100K \leq T_{\rm eff} < 6000K$, and $\log\ g > 4.0$) in Q0-Q6. The error bar for each bin was calculated by taking the square root of the sum of the squared weights in that bin . (a) Distribution of the number of observed super-flares per recorded flare peak amplitude. (b) Distribution of flare frequency as a function of flare energy. The distributions of all stars and slowly rotating stars are shown by solid and dashed lines, respectively. All G-type dwarfs and slowly rotating G-type dwarfs have power-law indices of 2.2 and 2.0, respectively. (c) Distribution of flare frequency as a function of flare energy of all cool stars ($5100K \leq T_{\rm eff} < 5600K$, grey-dashed histogram), and all hot stars ($5600K \leq T_{\rm eff} < 6000K$ white-solid histogram) (d) The same as (c), but for flares on slowly rotating stars $P_{\rm rot} > 10$ days. The average energy of the two red bins were used to calculate the occurrence frequency of super flares with energy of 2.11×10^{35} erg. (e) and (f) are the comparisons between the findings of this study and those of Shibayama et al. (2013) on all G-type dawarfs and Sun-like stars, respectively.

of super-flares as a function of energy on all cool G-type dwarf with $5100K \leqslant T_{\rm eff} < 5600K$ (grey-dashed histogram) with 255 observed super-flares, and all hot G-type dwarfs with $5600K \leqslant T_{\rm eff} < 6000K$ (white-solid histogram) with 1043 observed super-flares. Figure 6(d) the same as 6(c) but for slowly rotating G-type dwarfs with rotation period more than 10 days. The number of observed super-flares for cool slowly rotating G-type dwarfs is 78, and 151 for hot slowly rotating G-type dwarfs (Sun-like stars). From the two figures, we find that the frequency of super-flares is higher in cool G-type dwarfs than in hot G-type dwarfs, again confirming the previous results of (Maehara et al. 2012; Shibayama et al. 2013). Note that the difference in the occurrence rate of super-flares between the cool and hot stars in this study is not as large as in (Maehara et al. 2012; Shibayama et al. 2013). We can explain this by noting that our sample's number

Table 3. The number of observed G-type stars N_{os} distributed according to their effective temperature T_{eff} and rotational period P_{rot}.

T_{eff} K	N_{os}	Slow $P_{rot} > 10$ d	Fast $P_{rot} \leq 10$ d
5100-5600	3839	3518	321
5600-6000	21603	19160	2443
Total	25442	22678	2764

of cool stars constitutes approximately 15.1% of the total number of the sample while hot stars make up 84.9% of the total number of the sample, see table 3. In contrast, in Shibayama et al. (2013), cool stars make up about 48.7% of the total number of the sample, and hot stars constitute 51.3% of the total number of the sample. In addition, if we compare the number of superstars relative to the observed stars, we find that this rate is higher in cool stars than in hot ones, see columns 5, 8 and 13 in table 5.

We calculated the occurrence frequency rate of super-flares from the number of observed super-flares N_f, the number of observed stars N_{os} and the observation duration D (Maehara et al. 2012; Shibayama et al. 2013). The super-flares energy distribution in Q0-Q6, which ranges from 2.84×10^{33} erg to 2.94×10^{36} erg, varies from Q7-Q17 and Q0-Q17, which ranges from 2×10^{33} erg to 1.42×10^{38} erg, resulting in a different energy bins distribution. Therefore, in order for the energy used to derive the occurrence frequency rate of super-flares to be close for each section of the analysis (Q0-Q6, Q7-Q17 and Q0-Q17), we used the average energy of the two red bins in 6(d), which equals 2.11×10^{35} erg and is close to the energy 2.26×10^{35} erg that used in Q7-Q17 and Q0-Q17, red bins in Figures 7(d) and 8(d). As a result, the rate of super-flares incidence with energy of 2.11×10^{35} erg is 2.46×10^{-4} flares per year per star, corresponding to a super-flare occurring on a star once every 4070 years. This result is within about 80% of the occurrence rate of super-flares with energy of 10^{35} erg found by Shibayama et al. (2013), which equals to one super-flare in 5000 years for each star. Figures 6(e) and 6(f) show a comparison between the results of this study (solid-white-histogram) and Shibayama et al. (2013) study (grey-dashed-histogram). Figure 6(e) depicts the frequency distribution of super-flares energy for all G-type dwarfs, $dN/dE \propto E^{-\alpha}$, where $\alpha \sim 2.2$ in each of the two studies. 6(f) show the same comparison but for Sun-like stars with 151 super-flares in this study and 44 super-flares in Shibayama et al. (2013). Note from the two comparisons that the estimated energy of super-flares in this study is higher than that of Shibayama et al. (2013). Our justification for this is related to the differences in the Kepler Data Release between DR 9 and DR 25 used in Shibayama et al. (2013) and this study, respectively. Since the Kepler pipeline was updated between DR 9 and DR 25, PDC light curves for each target may also be updated. Also, the previous work may have used a slightly different parameters since the effective temperature and radius of some Kepler targets have been updated since then, resulting in different Kepler IDs for each spectral type. Another factor that may affect the energy value is that in this study, we used the flux difference rather than the flux to determine the start time of the flare. This can result in an extra data point between the flare's start and end times, resulting in higher energy. To find how our method affects the energy calculation results, we run the script on 279 flare stars from Shibayama et al. (2013) in order to compare the energy results drived form the script with those in Shibayama et al. (2013). We found 503 common super-flares with the same start-time of the flare between Shibayama et al. (2013) and our script result. Then we calculated correlation coefficient between the energy values and we observed an energy increase for our study, with a correlation coefficient of 0.66 between the two energies. Such small correlation coeffieint points to a sizeable difference the flare energy estimates between this study and Shibayama et al. (2013), for the reasons listed above.

4.1.2 *Super flares on G-type dwarfs in Q7-Q17*

We detected 3339 super-flares on 1539 G-type dwarfs during the course of 930 days of continuous monitoring. 483 super-flares on 268 slowly rotating stars are among them. In the case of Sun-like stars, we found 288 super-flares on 180 of them. According to our findings, 318 G-type dwarfs out of 1539 exhibit several super-flares whereas 1221 show only one super-flare. A total of 38 out of 180 Sun-like stars have several super-flares, and 142 Sun-like stars have just one super-flare. The most powerful super-flare discovered during this period had an energy of 1.42×10^{38} erg, an amplitude of 22.75, and a duration of 0.06 days. Figure 7 depicts four log-log scale histograms displaying the frequency distribution of super-flares in quarters 7 to 17, similar to Figure 6, but without the comparisons in 6(e) and 6(f). The distribution of the number of observed super-flares per observed flare peak amplitude is shown in Figure 7(a). The total number of super-flares detected is 3339, with amplitudes ranging from 7.5×10^{-4} to 35. Figures 7(b,c and d) have similar format as Figures 6(b,c and d). A comparison of super-flare frequency distributions on all G-type dwarfs (white-solid histogram) and slowly rotating G-type dwarfs (grey-dashed histogram) is shown in Figure 7(b). The power-law index for super-flare frequency distributions on all G-type dwarfs $\alpha \simeq 2.2 \pm 0.1$ and for slowly rotating G-type dwarfs $\alpha \simeq 2.1 \pm 0.4$. Figures 7(c) and 7(d) show the distribution of super-flares as a function of flare's energy according to the effective temperature of the star for all G-type dwarfs and slowly rotating G-type dwarfs respectively. where the number of detected super-flares is 642 super-flares on all cool G-type dwarf (grey-dashed histogram) and 2697 super-flares on all hot G-type dwarfs (white-solid histogram) in 7(c) and 195 super-flares on cool slowly rotating G-type dwarfs (grey-dashed histogram) and 288 super-flares on hot slowly rotating G-type dwarfs (white-solid histogram) in 7(d). The red bin in 7(d) shows that the occurrence frequency rate of super-flares with energy of 2.26×10^{35} erg is 1.31×10^{-4} flares per year per star, corresponding to a super-flare occurring on a star once every 7640 years. We note that this value is somewhat larger that similar results for Q0-Q6 and Q0-Q17.

4.1.3 *Super flares on G-type dwarfs in Q0-Q17*

Combining the two previous observations, we find that during 1424 days of continuous monitoring, we found 4637 super-flares on 1896 G-type dwarfs. Among them are 712 super-flares on 355 slowly rotating stars. We discovered 439 super-flares on 243 of the Sun-like stars. Our findings suggest that 397 stars out of 1896 G-type dwarfs have more than one super-flares, whereas 1499 stars have only one super-flare. A total of 55 out of 243 Sun-like stars have several super-flares, whereas 188 Sun-like stars have just one super-flare. Table 4 lists some super-flares stars with their parameters and the number of occurred super-flare N_f. The entire results can be found at `https://github.com/akthukair/AFD`. Figure 8 similar to Figure 7 shows four log-log scale histograms of the frequency distribution of super-flares as a function of flare energy in quarters 0 to 17. Figure 8(a) shows the distribution of the number of observed super-flares per observed flare peak amplitude. The amplitude of the 4,637 detected super-flares ranges between 7.5×10^{-4} and 35.6. Figure 8(b, c, and d) format is similar to Figure 7(b, c and d). Figure 8(b) compares the

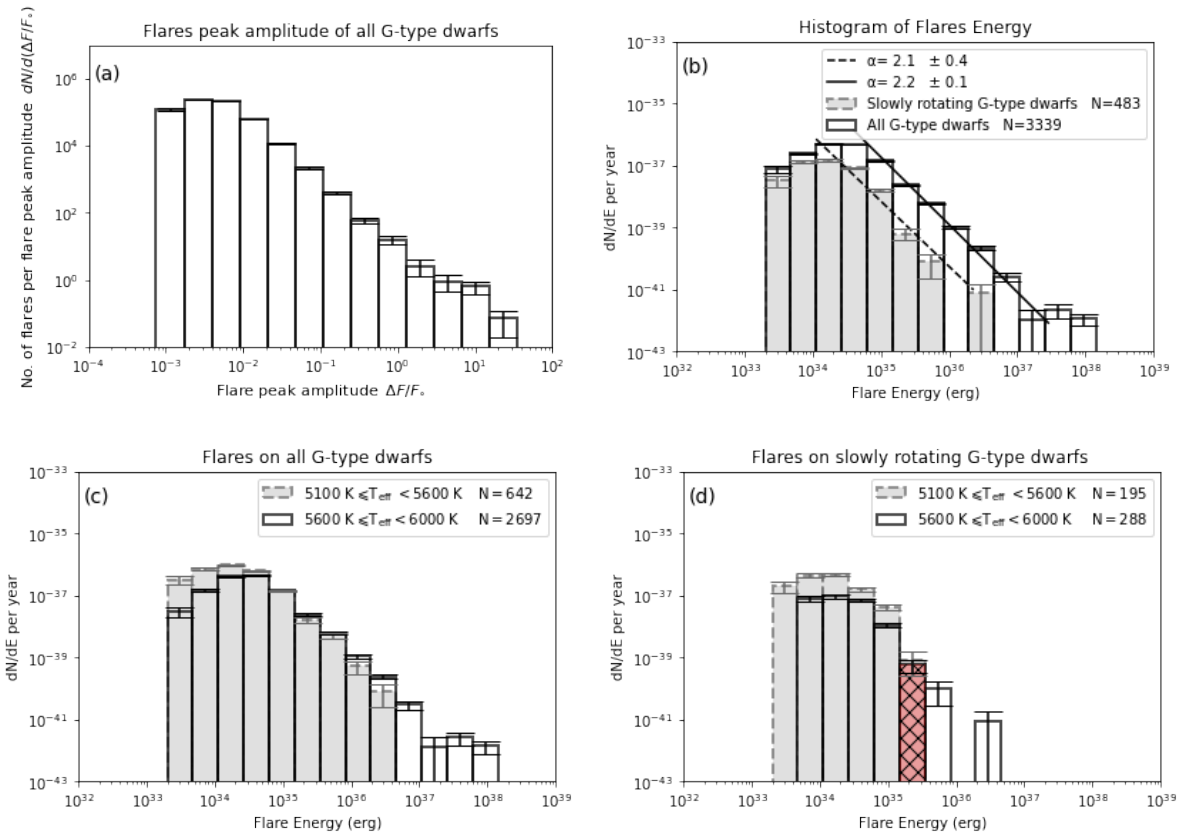

Figure 7. The same as in Figure 6 (a-d) but for Q7-Q17 data. The flare frequency distribution in (b) for all G-type dwarfs and slowly rotating G-type dwarfs have power-law indices of 2.2 and 2.1, respectively. The red bins in (d) were used to calculate the occurrence frequency of super flares with energy of 2.26×10^{35} erg.

frequency distributions of super-flares on all G-type dwarfs (white-solid histogram) and slowly rotating G-type dwarfs (grey-dashed histogram). Super-flare frequency distributions on all G-type dwarfs have a power-law index of $\alpha \simeq 2.0 \pm 0.1$, while slowly rotating G-type dwarfs have a power-law index of $\alpha \simeq 2.2 \pm 0.3$. A comparison of the distribution of super-flares as a function of flare energy for all G-type dwarfs and slowly rotating G-type dwarfs, according to the effective temperature of the star are shown in Figures 8(c) and (d). In Figure 8(c), there are 897 super-flares on all cool G-type dwarfs (grey-dashed histogram) and 3740 super-flares on all hot G-type dwarfs (white-solid histogram), 273 super-flares on cool slowly rotating G-type dwarfs (grey-dashed histogram) and 439 super-flares on hot slowly rotating G-type dwarfs (white solid histogram) (d). The occurrence frequency rate of super-flares with energy equal to 2.26×10^{35} erg is 2.29×10^{-4} flares per year per star, corresponding to a super-flare occurring on a star once every 4360 years, as shown in the red bin in Figure 8(d).

4.2 Super flares on other spectral type stars

We detected a total of 11438 super-flares on 1740 stars of other spectral types during 1424 days of continuous observation of dwarfs of 2653 A-type, 10898 F-type, 10307 K-type and 2222 M-type. The entire results can be found at `https://github.com/akthukair/AFD`.

For A-type dwarfs, we found 321 super-flares on 136 stars; 44 of these stars show more than one super-flare and 92 stars show only one super-flare. The duration of these super-flares can be up to 0.27 days, their flare maximum amplitude is 0.47. The largest flare energy we have determined is 8.91×10^{37}erg, with an amplitude of 0.28, and it lasted for 0.16 days.

As for F-type dwarfs, we discovered 1125 super-flares on 522 stars; 106 of these stars exhibit several super-flares, whereas 416 stars exhibit only one. These super-flares duration can be up to 0.57 days, and their flare amplitude can reach 0.08. Our calculations show that the highest flare energy we have found was 2.35×10^{36}erg, had an amplitude of 0.036, and lasted for 0.2 days.

Moving on to K-type dwarfs, we detected 4538 super-flares on 770 stars; 304 show several super-flares, while 466 stars show just one. The duration of these super-flares can be up to 0.3 days, and their amplitude can reach 1.04. The largest flare energy we have measured is 2.82×10^{36}erg, with an amplitude of 0.057 and a duration of 0.28 days.

For M-type dwarfs, we found 5445 super-flares on 312 stars; 256 of which have several super-flares and 56 have only one. These super-flares duration can be up to 0.82 days, and their flare amplitude varies between 0.002 to 15.1. The highest flare energy we have recorded was 1.59×10^{35}erg, has an amplitude of 15.1 and a duration of 0.18 days.

Figure 9 shows the flares frequency distribution on different spectral types, which follows a power-law relation ($dN/dE \propto E^{-\alpha}$). We used roughly the same energy range to obtain the best fit for α index in order to compare between the results. In order to maintain accurate statistics, we disregarded bins at the end of the histogram that contain a small number of flares (five or less).

Yang & Liu (2019b) reported a total of 162,262 flare events on

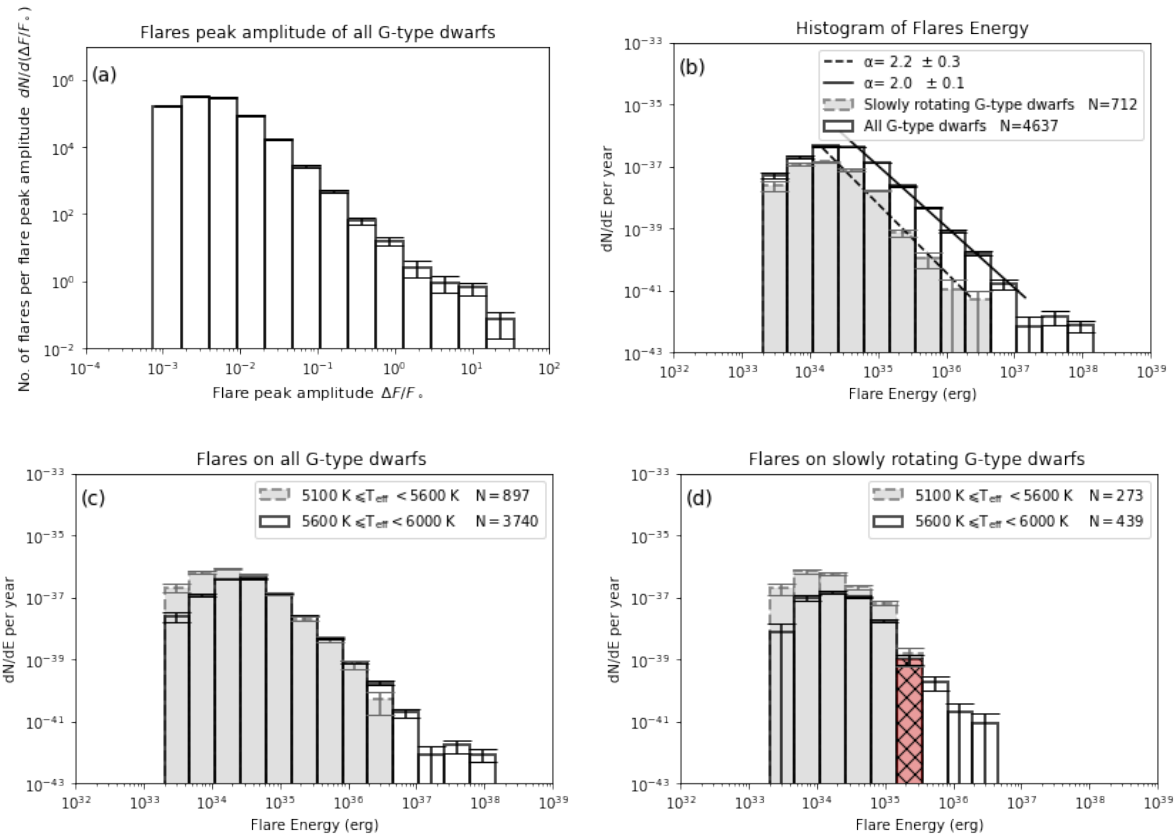

Figure 8. The same as in Figures 6 (a-d) and 7 but for Q0-Q17 data. The flare frequency distribution in (b) for all G-type dwarfs and slowly rotating G-type dwarfs have power-law indices of 2.0 and 2.2, respectively. The red bins in (d) were used to calculate the occurrence frequency of super flares with energy of 2.26×10^{35} erg.

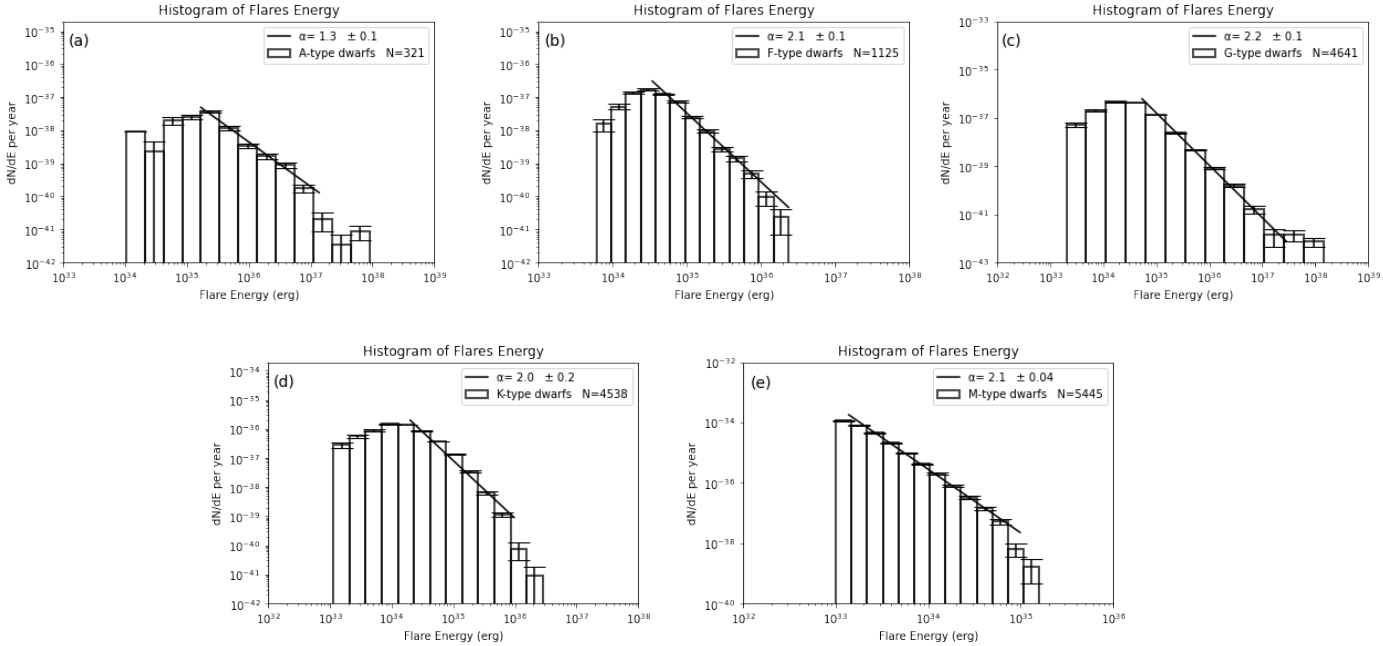

Figure 9. Log-log scale histograms showing the frequency distribution of super-flares organised by the stellar spectral type, with the α index of the power-law relation ($dN/dE \propto E^{-\alpha}$) and the number of super-flares for each spectral type indicated. We used approximately the same energy range for the fitting in all panels and ignored the bins towards the end of the histogram with a limited number of flares.

Table 4. The parameters of super-flare stars (G-type) with the number of flares N_f.

Kepler ID	T_{eff} (K)	log g	Radius ($R_\odot$)	P_{rot} (day)	N_f
1718360	5908	4.44	1.00	2	5
2302288	5904	4.45	1.01	9	1
2308761	5780	4.44	1.00	1	25
2445975	5780	4.44	1.00	1	9
2837133	5361	4.33	1.06	23	1
3852796	5650	4.37	0.98	11	2
3858729	5780	4.44	1.00	4	11
3869649	5525	4.46	0.90	1	13
4137840	5830	4.50	0.93	2	9
4346178	5392	4.31	1.09	34	3
4749912	5734	4.26	1.13	5	12
5105805	5849	4.52	0.92	13	2
5202404	5999	4.35	1.07	4	31
6223256	5951	4.30	1.11	2	38
6780893	5462	4.40	0.93	4	15
7958049	5802	4.38	0.94	2	97
8357647	5776	4.36	0.96	5	2
9390942	5999	4.49	0.96	8	1
9827094	5790	4.28	1.09	3	21
10518610	5530	4.43	1.02	18	1
10922936	5325	4.43	0.92	15	5
11809362	5216	4.45	0.90	15	1
11913716	5875	4.48	0.98	12	1
12266582	5638	4.39	0.93	6	4
12405306	5911	4.50	0.94	10	1

Note: The full version of the table is available at https://github.com/akthukair/AFD

3420 flaring stars. They found that the flare frequency distribution from F-type stars to M-type stars have an index $\alpha \sim 2$, while $\alpha \sim 1$ for the flares frequency distribution of A-type stars. In our study, we found that the α index is about 2 for spectral types from F-type to M-type stars. In particular $\alpha \simeq 2.1 \pm 0.1$ for F-type stars, $\alpha \simeq 2.0 \pm 0.1$ for G-type stars, $\alpha \simeq 2.0 \pm 0.2$ for K-type stars and $\alpha \simeq 2.1 \pm 0.04$ for M-type stars. These results are consistent with the previous results of Yang & Liu (2019b). Shibata et al. (2013) found that for the Sun-like stars, the flares frequency distribution of nanoflares, microflares, solar flares and superflares, follow a power-law relation with $\alpha \simeq 1.8$. It means that the underlaying mechanism which is generating these flares by magnetic reconnection occurs in similar physical conditions Yang & Liu (2019b). It is thought that the same fundamental process that causes solar flares also causes flares in late-type stars (F-M). A convective envelope is necessary for the dynamo that generates the magnetic fields in these stars. For magnetic fields to become strong enough to rise and emerge into the stellar atmosphere, which results in the generation of flares, this convective envelope must be sufficiently deep Pedersen et al. (2017). The similarity of α index indicates that the process of producing flares in various spectral types from F-type to M-type stars is similar and is based on magnetic reconnection Yang & Liu (2019b).

However, the situation is different for A-type stars, as the α index for the flare frequency distribution differs from the rest and is $\alpha \simeq 1.3 \pm 0.1$. It is widely expected that these stars cannot have flares. For stars to produce flares, they must have a deep outer convection zone, powerful large-scale magnetic fields, or powerful winds produced by the radiation. Normal A-type stars are devoid of these characteristics. Hence they should not flare Pedersen et al. (2017). Moreover, According to stellar evolution theories, A-type stars are unlikely to flare because of their weak magnetic fields, and their thin or nonexistent surface convection zone, preventing a magnetic dynamo from operating Van Doorsselaere et al. (2017). However, through a visual inspection of the light curves, (Balona 2012, 2013) found flare events in the light curves of 33 A-type stars. To study the origin of these flares, Pedersen et al. (2017) reported a new, detailed analysis of these 33 A-type stars and verified the existence of flares in 27 of them. Balona (2015) observed 1833 and 424 A-type stars in long cadence and short cadence modes, respectively, during Q0-Q12 using visual inspection. In the long cadence and short cadence modes, 51 and 10 A-type stars, respectively, show evidence of flare activity. Moreover, 24 new A-type stars with flaring activity have been discovered by Van Doorsselaere et al. (2017).

Table 6 shows the number of super-flares for each spectral type. Where $N_{f\ (candidates)}$ is the number of flares candidates captured by the code when the flux difference exceeded the threshold limit, $N_{f\ (conditions)}$ is the number of flares that met all the conditions, $N_{f\ (check)}$ is the number of flares we verified using visual inspection of the light curves, and $N_{f\ (exclude)}$ is the number of flares that we excluded due to their irregular, chaotic shape after the visual inspection of the light curves. By analyzing this table, we notice a large fraction of excluded flares are in the A-type stars compared to the M-type stars. This can be explained by the different flare conditions in the stars. One difference can be that the sizes of A-type star-spots are much larger than that of M-type, with different magnetic reconnection conditions, resulting in the flares with irregular, chaotic shapes of the light curves in A-type stars. This is possibly why A-type stars have a different α index. Table 7 shows the incidence of flares for each stellar spectral type. Since our study considers main-sequence stars only, the number of stars is limited to a specific radius range for each spectral type, and therefore the number of stars in this study is much smaller than in other studies such as Yang & Liu (2019b). Thus the flare incidence appears in larger numbers than in those studies. The flare incidence gradually increases from F-type to M-type stars from 4.79 % to 14.04 % because of the increase of the convection zone depth Yang & Liu (2019b). However, the incidence of the flares in A-type stars 5.13 % is higher than in F-type stars 4.79 %, which contradicts the theoretical expectation. As from an A-type star to an F-type star, a star's outer layer changes from the radiative envelope to the convective envelope, allowing F-type stars to operate a solar-like dynamo. In contrast, A-type stars struggle to create and maintain a magnetic field Yang & Liu (2019b). These results are also consistent with (Balona 2015; Van Doorsselaere et al. 2017; Yang & Liu 2019b), who analyzed stars of any size, not just those on the main-sequence discussed here. The deviation of the α index in A-type stars from the rest of stellar types, the rise of flare incidence rate compared to F-type stars, and the high percentage of excluded flares compared to the rest of the spectral types are all indications that A-type stars may generate flares in a different, peculiar manner.

5 CONCLUSION

Using bespoke Python script written by us, we performed an automated search for super-flares on main-sequence stars of types A, F, G, K, and M in all of Kepler's long-cadence data of DR 25 from Q0 to Q17, using Shibayama et al. (2013) technique. We used the Harvard Spectral classification to determine each target's spectral type based on its effective temperature and radius. For A, F, G, K and M type stars, we studied a total of 2653, 10898, 25442, 10307, and 2222 main-sequence stars, respectively. Consequently, we expanded earlier study of Shibayama et al. (2013), who only evaluated a smaller number of quarters (Q0-Q6) on G-type dwarfs only. As a result,

Table 5. The number of super-flares and super-flare stars.

Quarters	$T_{\rm eff}$	Slow			Fast			Unknown $P_{\rm rot}$		Total		
		$N_{\rm f}$	$N_{\rm fstar}$	$N_{\rm f}/N_{\rm os}$	$N_{\rm f}$	$N_{\rm fstar}$	$N_{\rm f}/N_{\rm os}$	$N_{\rm f}$	$N_{\rm fstar}$	$N_{\rm f}$	$N_{\rm fstar}$	$N_{\rm f}/N_{\rm os}$
0 – 6	5100 – 5600	78	39	0.02	141	35	0.43	36	30	255	104	0.07
	5600 – 6000	151	93	0.01	698	203	0.29	194	188	1043	484	0.05
7 – 17	5100 – 5600	195	88	0.06	303	59	0.94	144	116	642	263	0.17
	5600 – 6000	288	180	0.015	1552	361	0.64	857	735	2697	1276	0.12
0 – 17	5100 – 5600	273	112	0.08	444	65	1.38	180	141	897	319	0.23
	5600 – 6000	439	243	0.023	2250	653	0.92	1051	906	3740	1578	0.17

Note: $N_{\rm f}$ the number of super-flares, $N_{\rm fstar}$ the number of super-flare stars and $N_{\rm f}/N_{\rm os}$ the ratio of the number of super-flares to the number of observed stars $N_{\rm os}$. $N_{\rm os}$ can be found in table 3.

Table 6. The ratio rate of excluded flares for each spectral type.

Class	$N_{\rm f\ (candidates)}$	$N_{\rm f\ (conditions)}$	$N_{\rm f\ (check)}$	$N_{\rm f\ (exclude)}$	$N_{\rm f\ (exclude)}/N_{\rm f\ (conditions)}$
A	38876	953	321	632	66.32 %
F	187877	2484	1125	1359	54.71 %
G	481005	6791	4637	2154	31.72 %
K	207205	6754	4538	2216	32.81 %
M	15165	6808	5445	1363	20.02 %

Note: $N_{\rm f\ (candidates)}$ represents the number of flare candidates captured by our Python code when the flux difference exceeds the threshold limit. $N_{\rm f\ (conditions)}$ is the number of flares that satisfied all conditions, $N_{\rm f\ (check)}$ is the number of flares that were confirmed by visual examination of the light curves. Following a visual examination of the light curves, $N_{\rm f\ (exclude)}$ is the number of flares that were excluded due to their irregular, chaotic shape.

Table 7. The number of stars $N_{\rm star}$, flare stars $N_{\rm fstar}$ and flare incidence for each spectral type.

Class	$T_{\rm eff}$ (K)	Radius ($R_\odot$)	$N_{\rm star}$	$N_{\rm fstar}$	incidence
A	7500 - 10000	1.4 - 1.8	2653	136	5.13 %
F	6000 - 7500	1.15 - 1.4	10898	522	4.79 %
G	5100 - 6000	0.9 - 1.15	25442	1896	7.45 %
K	3700 - 5200	0.7 - 0.96	10307	770	7.47 %
M	2400 - 3700	$\leqslant 0.7$	2222	312	14.04 %

we detected 4637 super-flares on 1896 G-type dwarfs during 1424 days of continuous observation by Kepler. Using these new data, we studied and compared the statistical properties of the occurrence frequency rate of super-flares using three distinct datasets, namely, Q0-Q6, Q6-Q17, and Q0-Q17. According to our estimates for the Q0-Q17 dataset, a super-flare on G-type dwarfs with an energy of 10^{35} erg occurs on a star once every 4360 years. Moreover, we detected a total of 321, 1125, 4538 and 5445 super-flares on dwarfs of 136, 522, 770 and 312 A, F, K and M type stars respectively, during 1424 days of continuous observation. We determined the distributions of super-flare occurrence rates as a function of super-flare energy. We found that for all spectral types of stars, from F-type to M-type, the flare frequency distribution as a function of flare energy follows a power-law relation with $dN/dE \propto E^{-\alpha}$ where $\alpha \simeq 2.0$ to 2.1. This demonstrates that the power-law index α is similar to those of solar flares ($\sim$ 2) Shibayama et al. (2013). The power-law index values' similarity suggests that similar physical conditions produce the flares, by the mechanism which is thought to be magnetic reconnection. In contrast, the obtained value of α index 1.3 of the flare frequency distribution for A-type stars indicates that their flare conditions are distinct from those of the other stellar types. We observed a general rise in the flare incidence rate from 4.79 % and 14.04 % for F-type to M-type stars. However, the flare incidence rate is higher in A-type stars 5.13 % than in F-type stars 4.79 %, contrary to the theoretical expectation Yang & Liu (2019b). These results are similar to those found by (Balona 2015; Van Doorsselaere et al. 2017; Yang & Liu 2019b)

ACKNOWLEDGEMENTS

Some of the data presented in this paper were obtained from the Mikulski Archive for Space Telescopes (MAST). STScI is operated by the Association of Universities for Research in Astronomy, Inc., under NASA contract NAS5-26555. Support for MAST for non-HST data is provided by the NASA Office of Space Science via grant NNX13AC07G and by other grants and contracts.

Authors would like to thank Deborah Kenny of STScI for kind assistance in obtaining the data, Cozmin Timis and Alex Owen of Queen Mary University of London for the assistance in data handling at the Astronomy Unit.

A. K. Althukair wishes to thank Princess Nourah Bint Abdulrahman University, Riyadh, Saudi Arabia and Royal Embassy of Saudi Arabia Cultural Bureau in London, UK for the financial support of her PhD scholarship, held at Queen Mary University of London.

REFERENCES

Balona L. A., 2012, MNRAS, 423, 3420
Balona L. A., 2013, MNRAS, 431, 2240
Balona L. A., 2015, MNRAS, 447, 2714
Breton S. N., Santos A. R. G., Bugnet L., Mathur S., García R. A., Pallé P. L., 2021, A&A, 647, A125
Bryson S. T., et al., 2010, in Radziwill N. M., Bridger A., eds, Society of Photo-Optical Instrumentation Engineers (SPIE) Conference Series Vol. 7740, Software and Cyberinfrastructure for Astronomy. p. 77401D, doi:10.1117/12.857625
Caldwell D. A., et al., 2010, in Space Telescopes and Instrumentation 2010: Optical, Infrared, and Millimeter Wave. pp 343–353
Carrington R. C., 1859, MNRAS, 20, 13
Davenport J. R. A., 2016, ApJ, 829, 23
Eastwood J. P., et al., 2017, Risk Analysis, 37, 206
Günther M. N., et al., 2020, The Astronomical Journal, 159, 60
Hawley S. L., Fisher G. H., 1992, ApJS, 78, 565
Koch D. G., et al., 2010, The Astrophysical Journal Letters, 713, L79
Kretzschmar M., 2011, A&A, 530, A84
Maehara H., et al., 2012, Nature, 485, 478

Masuda S., Kosugi T., Hara H., Tsuneta S., Ogawara Y., 1994, Nature, 371, 495
Mathioudakis M., Seiradakis J. H., Williams D. R., Avgoloupis S., Bloomfield D. S., McAteer R. T. J., 2003, A&A, 403, 1101
Mathioudakis M., Bloomfield D. S., Jess D. B., Dhillon V. S., Marsh T. R., 2006, A&A, 456, 323
McQuillan A., Mazeh T., Aigrain S., 2014, ApJS, 211, 24
Namekata K., et al., 2017, ApJ, 851, 91
Nielsen M. B., Gizon L., Schunker H., Karoff C., 2013, A&A, 557, L10
Notsu Y., Maehara H., Shibayama T., Honda S., Notsu S., Namekata K., Nogami D., Shibata K., 2016, in 19th Cambridge Workshop on Cool Stars, Stellar Systems, and the Sun (CS19). Cambridge Workshop on Cool Stars, Stellar Systems, and the Sun. p. 119 (arXiv:1608.00186), doi:10.5281/zenodo.59138
Ofman L., Averbuch A., Shliselberg A., Benaun I., Segev D., Rissman A., 2022, New Astron., 91, 101693
Pedersen M. G., Antoci V., Korhonen H., White T. R., Jessen-Hansen J., Lehtinen J., Nikbakhsh S., Viuho J., 2017, MNRAS, 466, 3060
Pettersen B. R., 1989, Sol. Phys., 121, 299
Pitkin M., Williams D., Fletcher L., Grant S. D. T., 2014, MNRAS, 445, 2268
Reinhold T., Gizon L., 2015, A&A, 583, A65
Santos A. R. G., García R. A., Mathur S., Bugnet L., van Saders J. L., Metcalfe T. S., Simonian G. V. A., Pinsonneault M. H., 2019, ApJS, 244, 21
Santos A. R. G., Breton S. N., Mathur S., García R. A., 2021, ApJS, 255, 17
Schulte in den Bäumen H., Moran D., Lenzen M., Cairns I., Steenge A., 2014, Natural Hazards and Earth System Sciences, 14, 2749
Schüssler M., Solanki S., 1992, Astronomy and Astrophysics, 264, L13
Shibata K., Magara T., 2011, Living Reviews in Solar Physics, 8, 6
Shibata K., Masuda S., Shimojo M., Hara H., Yokoyama T., Tsuneta S., Kosugi T., Ogawara Y., 1995, The Astrophysical Journal, 451
Shibata K., et al., 2013, PASJ, 65, 49
Shibayama T., et al., 2013, The Astrophysical Journal Supplement Series, 209, 5
Van Cleve J., Caldwell D., 2009, Technical report, Kepler Instrument Handbook (KSCI-19033-001). KSCI-19033-001. pdf
Van Doorsselaere T., Shariati H., Debosscher J., 2017, ApJS, 232, 26
VanderPlas J. T., 2018, ApJS, 236, 16
Vida K., Roettenbacher R. M., 2018, A&A, 616, A163
Walkowicz L. M., et al., 2011, AJ, 141, 50
Yang H., Liu J., 2019a, VizieR Online Data Catalog, p. J/ApJS/241/29
Yang H., Liu J., 2019b, ApJS, 241, 29
Yang H., et al., 2017, The Astrophysical Journal, 849, 36

This paper has been typeset from a TEX/LATEX file prepared by the author.